Science Advances
AAAS

advances.sciencemag.org/cgi/content/full/4/11/eaas9530/DC1

Supplementary Materials for

Toward all-day wearable health monitoring: An ultralow-power, reflective organic pulse oximetry sensing patch

Hyeonwoo Lee, Eunhye Kim, Yongsu Lee, Hoyeon Kim, Jaeho Lee, Mincheol Kim, Hoi-Jun Yoo, Seunghyup Yoo*

*Corresponding author. Email: syoo.ee@kaist.edu

Published 9 November 2018, *Sci. Adv.* **4**, eaas9530 (2018)
DOI: 10.1126/sciadv.aas9530

This PDF file includes:

Supplementary Materials

Section S1. Device characteristics of OLEDs and OPDs

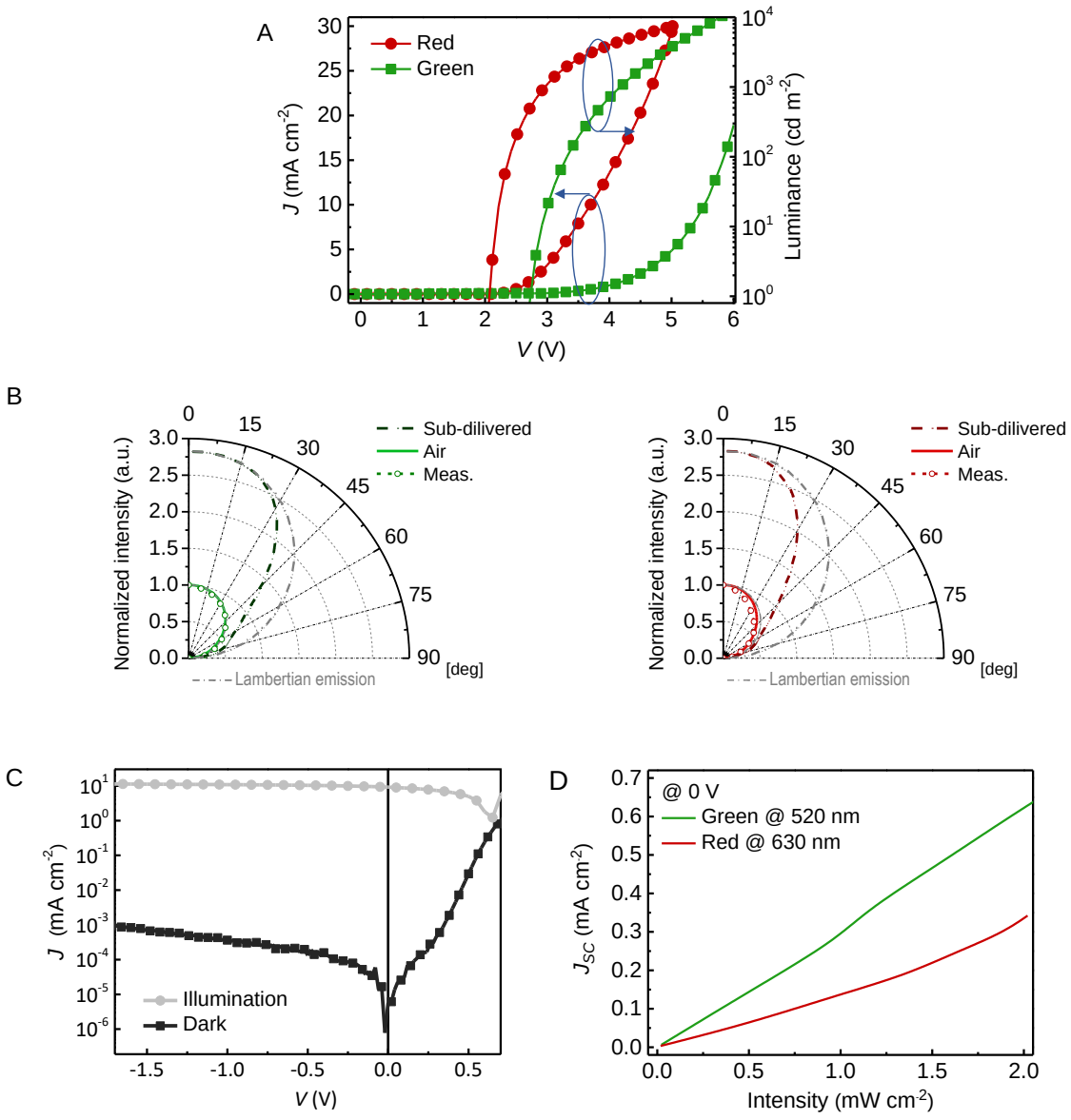

Fig. S1. Opto-electrical characteristics of OLEDs and OPDs used in this work. (**A**) *J-V-L* characteristics of green and red OLEDs. (**B**) Angular intensity characteristics of green OLEDs (left) and red OLEDs (right). The measured and simulated values are provided for the light coupled to air, and the simulated values are provided for the light coupled to a substrate before it is outcoupled to air. (**C**) *J-V* curves of OPDs under illumination (AM 1.5G) and in dark. (**D**) Short circuit current (J_{sc}) versus the light intensity of green and red OLEDs at zero voltage bias.

[Further note on estimating D^* of the OPD under study]

The specific detectivity (D^*) is a parameter characterizing the performance of a photodiode. It is defined as the reciprocal of a noise-equivalent power (NEP) with the effect of device area (A_{PD}) and the frequency bandwidth (f) normalized

$$D^*(\lambda) = \frac{1}{NEP/\sqrt{Af}} = \frac{\sqrt{Af}}{I_{tn}/R_{PD}(\lambda)} = \frac{R_{PD}(\lambda)\sqrt{Af}}{I_{tn}} \qquad \text{(Eq. S1)}$$

where I_{tn} is the total noise current and $R_{PD}(\lambda)$ is the responsivity of a photodetector (given in the unit of A/W) at the wavelength of λ. The second relation in Eq. S1 is derived from the fact that NEP is defined as the optical power incident on the PD under test that corresponds to the case where the photo-generated current $I_{ph} = I_{tn}$.

When I_{tn} consists only of thermal or Johnson noise (I_{jn}) and shot noise (I_{sn}), Eq. S1 can be expressed as follows

$$D^*(\lambda) = \frac{R_{PD}(\lambda)\sqrt{Af}}{\sqrt{\frac{4k_BT}{R_p}f + 2e\left(I_{dark} + I_{ph}\right)f}} = \frac{R_{PD}(\lambda)}{\sqrt{\frac{4k_BT}{R_pA} + 2e\left(J_{dark} + J_{ph}\right)}} \qquad \text{(Eq. S2)}$$

where J_{dark} and J_{ph} are the dark and photo-generated current density, respectively, and A, R_p and k_B are the device area and the shunt resistance of the PD, and Boltzmann constant, respectively.

In an 'ideal' situation where a detector can be cooled down and thus Johnson noise becomes negligible, D^* is limited only by the shot noise. When the condition $I_{tn} = I_{sn} = I_{ph}$ is met, I_{ph} is much smaller than I_{dark} for most practical range of the frequency bandwidth; hence D^* for the ideal shot-noise limited case is obtained with T=0 and $J_{ph} << J_{dark}$ such that

$$D^*(\lambda) \approx D^*_{\text{ideal}}(\lambda) = \frac{R_{PD}(\lambda)}{\sqrt{2eJ_{dark}}} \qquad \text{(Eq. S3)}$$

The ideal situation is, however, mainly for comparison with other photodiode technologies and is hardly relevant to the present work where the sensor is attached to a human body, which is held at T = ca. 310K. When considering the

typical level of I_{ph} and R_p in the present case, Johnson noise dominates the shot noise, so that I_{tn} may be approximated to I_{jn}. In this 'typical' (Johnson-noise-limited) case

$$D^*(\lambda) \approx D^*_{Johnson}(\lambda) = \frac{R_{PD}(\lambda)}{\sqrt{\frac{4k_BT}{R_pA}}} \quad \text{(Eq. S4)}$$

The 'ideal' and 'typical' D^* values quoted at V = -60 mV of the proposed OPDs shown in Table 1 and in the main text were thus obtained with Eq. S3 and Eq. S4, respectively. The parameters used for Eq. S3 and Eq. S4 are summarized in table S1.

Table S1. Parameters used to estimate *D of the OPD under study.**

Case	**Major noise source**	R_pA **(Ωcm²)**	R_{PD} **(A/W)**	J_{dark} **(A/cm²) (at *V* = -60 mV)**	D^* **(cm · √Hz/W)**
Ideal	Shot noise	NA	0.29 (G) 0.21 (R)	1.4×10^{-8}	4.3×10^{12} (R) 3.1×10^{12} (G)
Typical	Johnson (thermal) noise at *T*=310K	205.9	0.29 (G) 0.21 (R)		3.2×10^{10} (G) 2.3×10^{10} (R)

Section S2. Detailed description on optical simulation

In this work, multi-layered human tissues were simplified as three layers which are composed of skin, subcutaneous tissues (fat), and muscle with different scattering and absorption coefficient for green and red spectra. The optical coefficients of those layers were taken from the literature. As the data in the literature were not always available throughout the spectrum, some data were taken at wavelengths that are different from the target wavelength but as close as possible. For example, the data for skin and subcutaneous tissues were from those specified at the wavelength (λ) of 520 nm and 610 nm wavelength while the data for muscle was from those obtained at λ of of 500nm and 650nm, respectively (*27, 28*). As for the phase function, which is the probability function of deflection angle per scattering, we have taken Henyey-Greenstein (H-G) phase function, which is popularly used in lieu of Mie scattering phase function for the sake of reducing the simulation load. The asymmetry parameter of H-G phase function was assumed to be 0.9, which is typically used for the analysis of tissues (*28*). The interface between substrates of OPO sensors and skin layers on contact was assumed to be index-matched at refractive index of 1.5 (*29*). Thickness of skin and fat was assumed 1.5 mm, respectively (*28, 38*) and thickness of muscle was set as 10 mm with infinite boundary; the relatively large thickness and infinite boundary for muscle prevents the light reaching the bottom of the muscle medium from returning. The emission from OLEDs were assumed as block sources where the rays were emitted from the designated area. The angular distribution of light emission from OLEDs coupled to substrates was assumed to be that of Lambertian source (*39*).

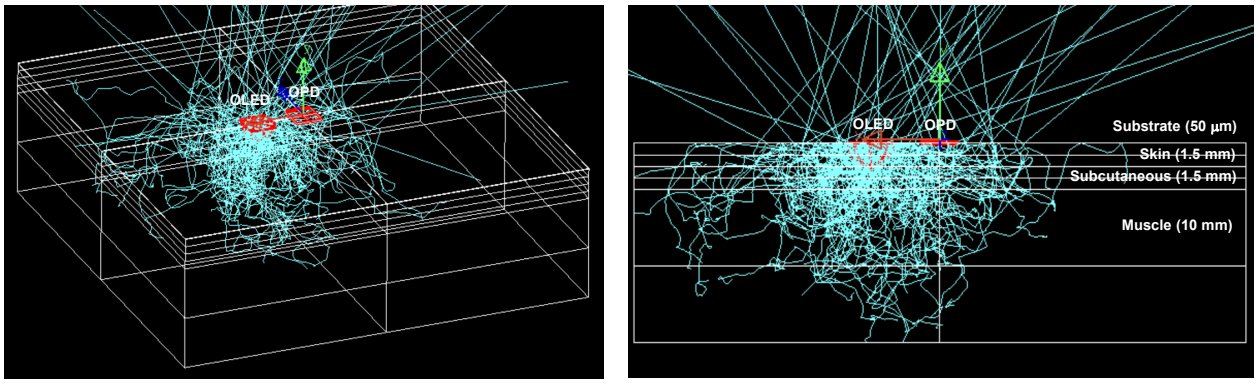

Fig. S2. Ray-tracing example of the proposed simulation model. The cyan lines correspond to the rays being traced.

Table S2. Optical parameter of the human skin layers applied to the simulation.

	Thickness (mm)	Color	μ_a (cm^{-1})	μ_s (cm^{-1})	g	n
Skin	1.5	G	1.41	34.4	0.9	1.5
		R	1.15	23.5		
Subcutaneous fat	1.5	G	1.14	14.8		
		R	1.14	12.8		
Muscle (infinite boundary)	10	G	1.2	68.7		
		R	0.56	64.7		

Section S3. Estimation of SNR ratio in a concentric configuration where a circular OLED is surrounded by a ring-type OPD sharing the center

Suppose $f_H(r)$, defined for $r \geq r_1$, is given by an exponential decay function as follows

$$f_H(r) = \gamma_1 \exp\left(-\frac{r-r_1}{l_0}\right) \quad \text{where } \gamma_1 \equiv f_H(r_1) \text{ given in the unit of } \mathrm{Wm}^{-2} \tag{Eq. S5}$$

The photocurrent generated by a ring-type OPD whose inner and outer radii are given by r_1 and r_2 is then given, under monochromatic assumption, by the following

$$\begin{aligned} I_{PH}{}^{(i)}(r_2) &= 2\pi\gamma_1 R_{PD}(\lambda_i)\int_{r_1}^{r_2} \exp\left(-\frac{r-r_1}{l_0^{(i)}}\right) r dr \quad \text{for } i = \text{R or G.} \\ &= 2\pi\gamma_1 R_{PD}(\lambda_i)\left(l_0^{(i)}\right)^2\left[\left(1-\frac{r_2}{l_0^{(i)}}\right)\exp\left(-\frac{r_2-r_1}{l_0^{(i)}}\right)-\left(1-\frac{r_1}{l_0^{(i)}}\right)\right] \end{aligned} \tag{Eq. S6}$$

The total noise current (I_{tn}) of the ring-type OPD is estimated, in consideration of both Johnson (thermal) noise and shot noise, by

$$\begin{aligned} &I_{tn} = \sqrt{I_{jn}{}^2 + I_{sn}{}^2} \\ &\text{where } I_{jn} = \sqrt{\frac{4k_B T}{R_p} f} \ , \quad I_{sn} = \sqrt{2e\left(I_{dark} + I_{PH}\right) f} \end{aligned} \tag{Eq. S7}$$

where k_B, e, I_{dark}, and f refer to Boltzmann constant, electronic charge, dark current, and frequency bandwidth, respectively.

Note that shunt resistance R_p and I_{dark} scales with $A_{PD}{}^{-1}$ and A_{PD}, respectively. Once they are measured at a given area A_{PD0} as R_{p0} and I_{dark0} , R_p and I_{dark} for A_{PD} are then give by

$$R_p = R_{p0}\frac{A_{PD0}}{A_{PD}} \quad , \qquad I_{dark} = I_{dark0}\frac{A_{PD}}{A_{PD0}} \tag{Eq. S8}$$

Plugging Eq. S4 into Eq. S3 leads to

$$I_{tn}(r_2) = \sqrt{\left(\frac{4k_B T}{R_{p0}A_{PD0}} + \frac{2eI_{dark0}}{A_{PD0}}\right) A_{PD}(r_2) f + 2eI_{PH}(r_2) f} \tag{Eq. S9}$$

It is noteworthy that I_{tn} scales approximately with $(A_{PD})^{0.5}$ for a wide range of r_2. On the other hand, as r_2 (and thus A_{PD}) increases, $I_{PH}(r_2)$ grows at a faster rate than $I_{tn}(r_2)$ when $(r_2\text{-}r_1) < l_0$, but it tends to grow slower than $I_{tn}(r_2)$ when

(r_2-r_1) >> l_0 . For this reason, SNR (=I_{PH}/I_{tn}) is maximized near $r_2 \sim r_1+\beta l_0$ where β is in the range of 1-2. The log-log plots obtained for I_{PH}, I_{tn}, and SNR vs. $A_{PD}(r_2)$ clearly show the expected tendency. It is noteworthy the slope of I_{tn} in the log-log plot is indeed 0.5, supporting the notion that I_{tn} scales with $A_{PD}^{0.5}$.

It is also noteworthy that SNR increases almost linearly with luminance (L) of a given OLED assuming the linear response of the OPD photocurrent (I_{ph}) to the irradiance, which is proportional to L. Note that the shot noise current (I_{sn}) scales with $I_{ph}^{0.5}$ and thus with $L^{0.5}$; however, the total noise (I_{tn}) is dominated mostly by the thermal noises and thus changes little with L in a typical temperature and brightness range. Therefore, SNR, determined by I_{ph}/I_{tn}, scales almost linearly with I_{ph} and thus L.

Different from the case of SNR, however, the light-penetration depth or the lateral propagation length does not vary depending on the luminance of a given OLED. The optimal value for r_2 may get affected due to the subtle change in balance between I_{ph} (r_2; L) and I_{sn} (r_2; L), but it turns out that it remains almost unchanged with respect to variation in luminance over ± two orders of magnitude from the case shown here.

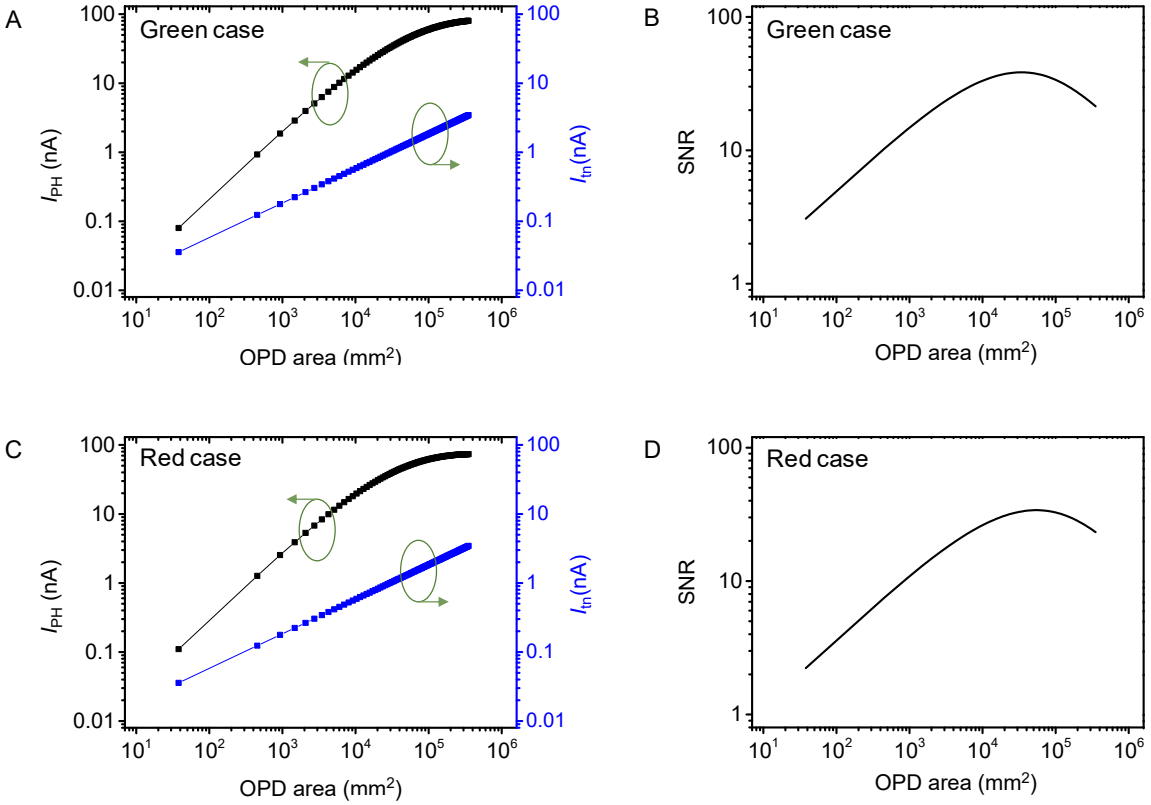

Fig. S3. Estimation of photo current, total noise, and SNR (= I_{PH}/I_{tn}) of each OLED case. (**A,B**) Estimated curve of green OLEDs case. (**C,D**) Estimated curve of red OLEDs case. (**A,C**) Estimation of the received photocurrent and noise current according to the area of OPD. (**B,D**) OPD area versus SNR curve from calculated photocurrent and total noise of OPD. The SNR values obtained here are with $f_H(r=r_1)$ and l_0 of 0.01W/m^2 and 2.25mm for red and 0.01W/m^2 and 1.75mm for green OLEDs.

Section S4. Summary of overall fabrication process and mask-in-mask concept used for precise alignment among different patterns during thermal evaporation

The overall fabrication process is summarized in Fig. S4A. All shadow masks were made of Invar (Fe-36Ni) steel, which can hold onto a magnet. First, we prepared 4 cm × 4 cm substrate pre-cuts on a plastic substrate with a laser cutter. We then fixed it onto a glass substrate used as a carrier that supports the plastic substrate between the shadow mask and the magnet. After that, we placed the first and second guide masks as shown in the first two photographs in Fig. S4B. Subsequently, the sub-mask for the IZO bottom electrode was fitted into the square opening of the second guide mask as shown in the third photograph in Fig. S4B (see description in the next paragraph and Fig. S4C for this "mask-in-mask" scheme,) After sputtering IZO electrodes, samples were loaded into a thermal evaporator, wherein thin films of organic and metal layers were deposited with proper sub-masks fitted into the square opening of the second guide mask for successive fabrication of an OPD, R OLED and G OLED. Once all the thermal evaporation processes are finished, samples were taken out from the vacuum chamber and went through encapsulation and interconnection (section S5).

Most thermal evaporation systems used in academia and research labs do not have vision systems for precise mask-to-mask alignment. This is all right for every-day fabrication of lab samples that typically involve device dimension of a few mm and alignment resolution on the order of 0.5 mm or larger. In the present work, however, the size of patterns and their alignment margins are so small that a conventional method cannot be used. We have thus devised a "mask-in-mask" scheme where a small mask with a desired pattern fits into a guide mask tightly as in a jigsaw puzzle, as shown in Fig. S4C. With the additional help of a magnet, the proposed method allowed us to have an alignment margin less than ca. 100 μm, making it easy to realize the optimal structure.

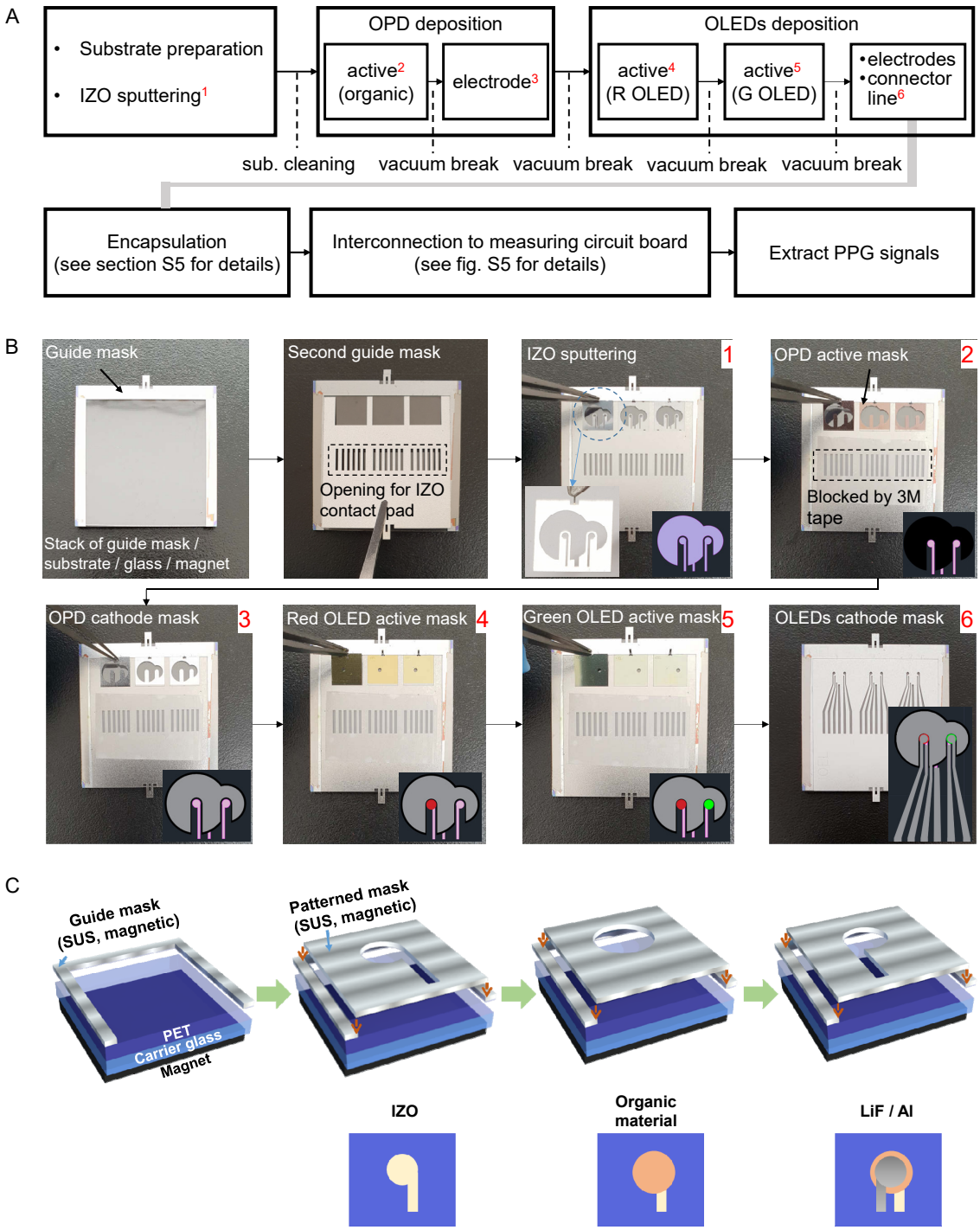

Fig. S4. Overview of fabrication process and pattern definition by jigsaw puzzle–type, mask-in-mask shadow masking method. (**A**) Schematic diagram of overall process for fabrication of the proposed OPO. (**B**) Photographs illustrating the "mask-in-mask" method used for deposition of constituent layers. The numbers in B in the right corner of each photograph indicate the processes in A marked with the corresponding numbers. The illustration at the bottom right of each photographs shows the pattern shape formed by each process step. The inset in left bottom corner of the photograph titled “IZO sputtering” is the photograph of the sub-mask used for IZO deposition. (**C**) A

process of a shadow mask alignment in which a patterned mask fits snuggly into a guide mask. Both the guide mask and the mask with a pattern are held tight with the help of a magnet. Between the deposition of organic layers and LiF/Al, vacuum of the deposition chamber is broken to change masks. During that time, samples are not exposed to ambient air but remain in inert atmosphere. Photo credit: Hyeonwoo Lee, KAIST.

Section S5. Face seal encapsulation and interconnection procedure and characteristics of encapsulated OLEDs and OPDs

Samples were packaged with a face-seal encapsulation following the procedure depicted in Fig. S5A. The face-sealed OLEDs and OPDs exhibited adequate shelf lifetime for testing outside the glovebox as shown in Figs. S5B and S5C. The anisotropic conductive film (ACF) provided by H&S HighTech Corp. was then used to connect the encapsulated OPOs to the flexible printed circuit board (FPCB) connectors. The ACF and FPCB are sequentially placed onto the electrode lines of the fabricated OPOs and pre-fixed with Kapton tapes, and then they were bonded with heat and pressure placed with the soldering iron. (See Fig. S5D-F.)

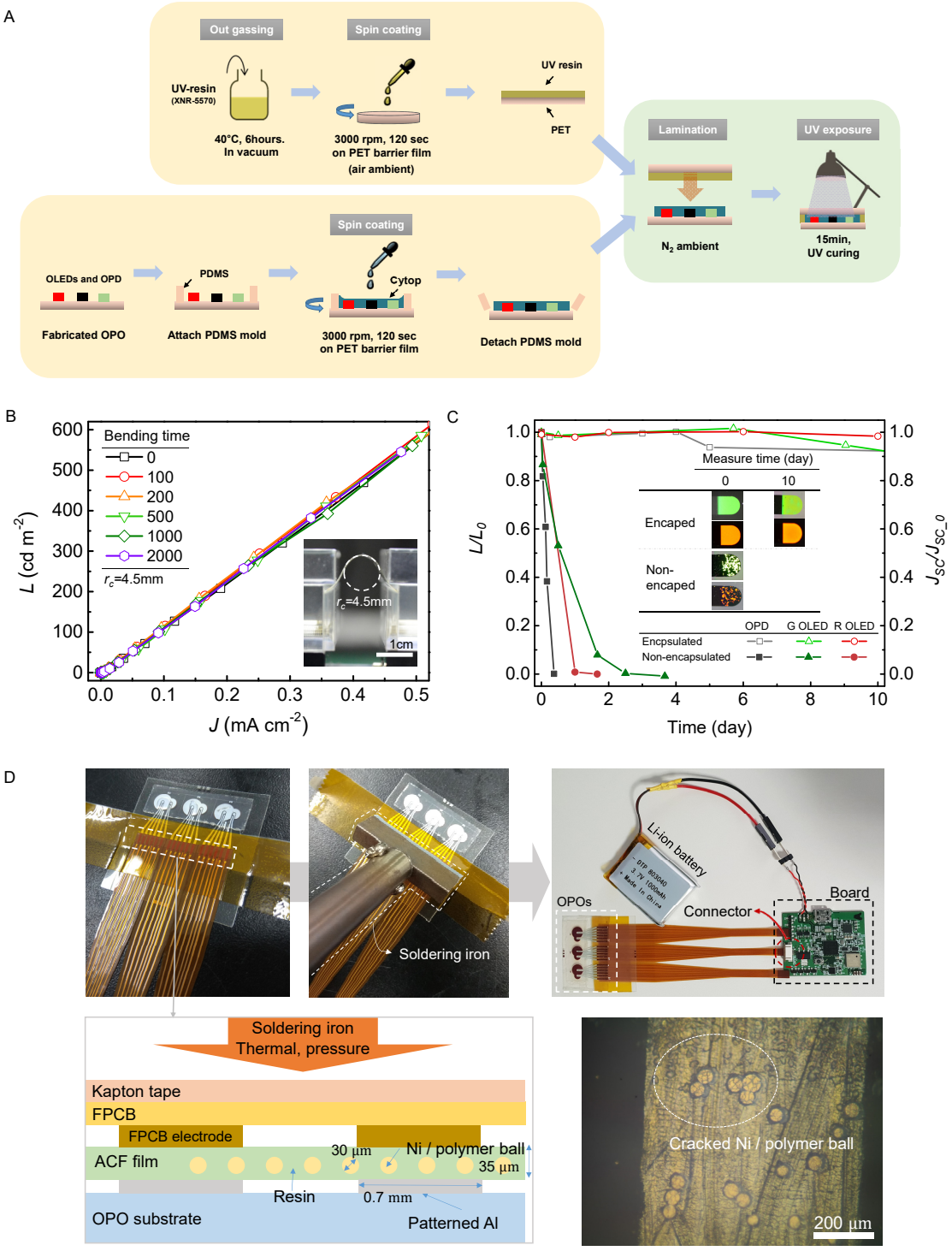

Fig. S5. Encapsulation and interconnection process and characteristics of the encapsulated devices. (**A**) The process of face-seal encapsulation used in this study. (**B**) Luminance versus current density curve that was measured after repeated bending cycles at radius of curvature (r_c) of 4.5 mm. Inset: the image of the OLED bent at r_c of 4.5 mm placed on a custom-built cyclic bending tester. (**C**) Normalized luminance of OLEDs and normalized short circuit current of OPDs (right column) measured as a function of storage time in 27 ºC, RH 47 %. Inset: the photographs of encapsulated or non-encapsulated OLEDs taken initially and after 10 days. (D) Photographs illustrating ACF-based

connection between the encapsulated OPOs and the circuit board. (E) Schematic cross-sectional view of the FBCB and OPO electrodes connection. (F) Microscopic image of a bonded connect line after bonding process. Cracked conductive balls in ACF can be seen. Photo credit: Hyeonwoo Lee, KAIST.

Section S6. Application of proposed OPOs onto various body parts

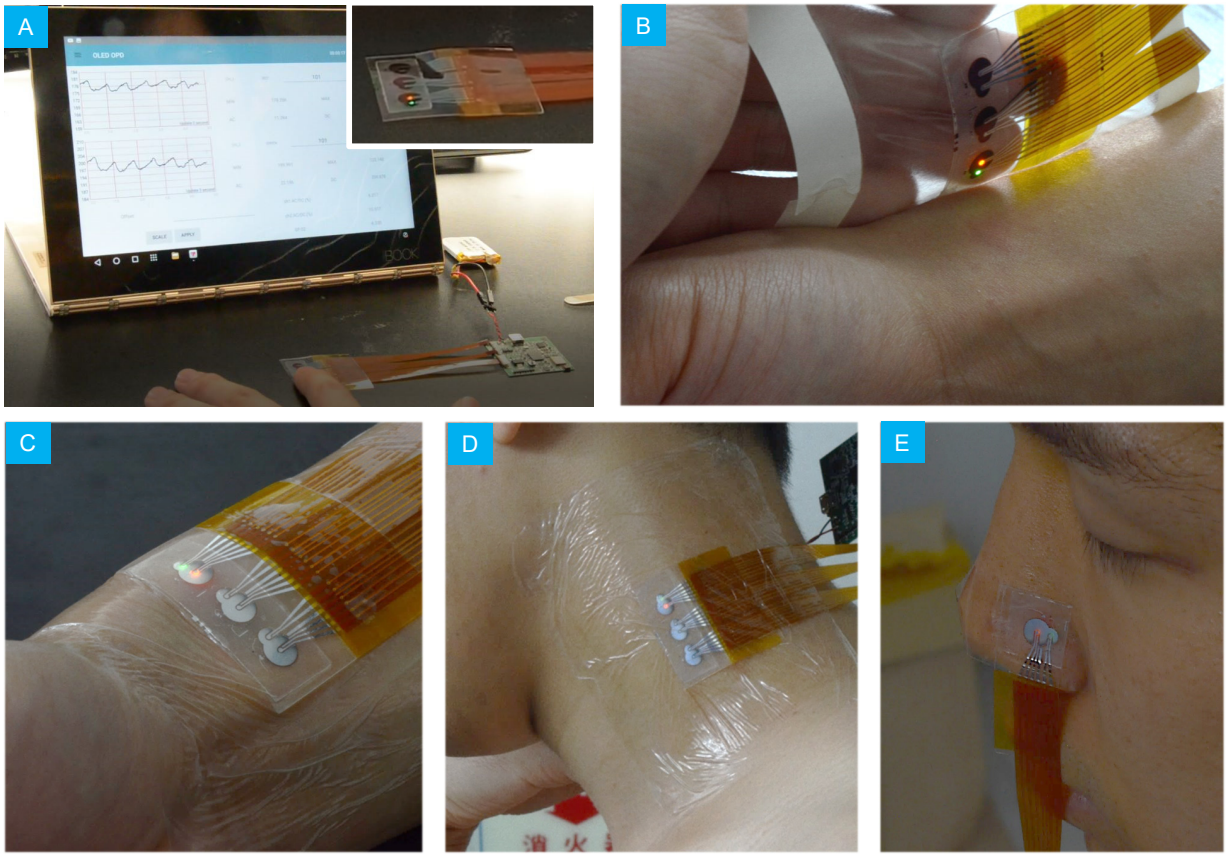

Fig. S6. Pictures of the working OPO sensors taken on the various body parts. (**A**) finger, (**B**) and (**C**) wrist, (**D**) neck, and (**E**) nose. Except for the finger, Tegaderm™ was used for stable attachment. The white strip shown in (B) is the liner of Tegaderm™, which is removed after attachment, For full conformal contact, the samples were gently pressed against the skin during the measurement. In (A), the photograph is presented for an OPO sensor, a control/ data acquisition board that communicates with a computer via wireless connection (Bluetooth). Photo credit: A. Haechang Lee, KAIST; B. Hyeowoo Lee, KAIST.

Section S7. Driving and signal acquisition scheme

The proposed OPO sensor board consists of three parts – 1) Power management unit (PMU), 2) Analog Front-end, and 3) Micro-controller unit (MCU) with communication module. PMU is implemented for generating three supply voltage domains from 3.7 V lithium-polymer battery. The boost converter with regulator generates 8 V for enough voltage headroom of OLEDs. Identical two buck converters with regulator make two 3.3 V domains for analog front-end and micro-controller unit with communication module, respectively. Analog and digital domain is separated for reducing noise effect during light signal sensing. Analog front-end is composed of two modules – OLED current driver and OPD receiver. OLED current driver can drive two OLEDs by turns, and current level is programmable from 10uA to 100mA with 8-bit resolution. OPD receiver with differential resistive-feedback trans-impedance amplifier (TIA) can amplify received light signal with programmable gain from 10 kΩ to 4 MΩ. The amplified analog signals are converted to digital data with 22-bit sigma-delta ADC. The dynamic range of OPD receiver is up to 105-dB.

Micro-controller receives the 22-bit data from analog front-end via serial peripheral interface (SPI) communication and transmit data via wired connection or wirelessly with Bluetooth module toward external devices (smart phone/computer). Micro-controller also adjusts several variables of analog front-end, not only receiving data. It controls current level and duty cycle of OLED driver to reduce power consumption. Furthermore, it adjusts the amount of rejected DC components in OPD receiver for wide dynamic range. The data sampling rate and sampling timing are also controlled with flexible clocking, the sampled frequency is variable from 62.5 HZ to 2000 Hz.

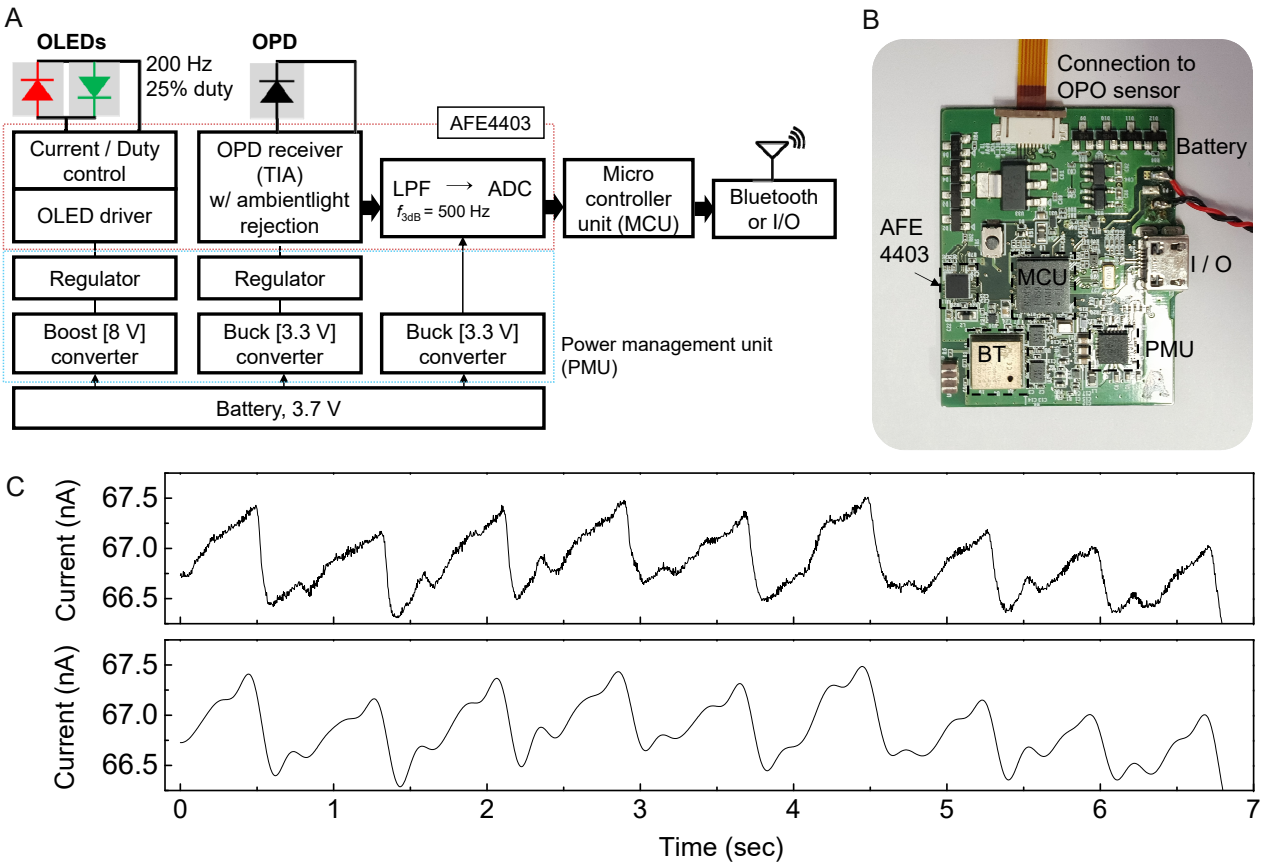

Fig. S7. Schematic diagram showing the circuit functional blocks for driving of OLEDs and signal acquisition from the OPD of the proposed OPO sensors. (**A**) Schematic diagram of OPOs measurement system. (**B**) The photograph of circuit board. For further details on circuitry, refer to Lee et al. (*14*). (**C**) Example of the experimental PPG signal after the output ADC stage of the circuit in A and its post-processed data based on a software-based low pass filter (LPF) having f_{3dB} of 5 Hz.

Section S8. SpO_2 calibration method for OPOs

In order to calibrate the SpO_2 value alteration with blood oxygen saturation of arterial blood (SaO_2), we performed the following procedure: A commercial pulse oximeter (CONTECTM, model: CMS50D+) is equipped on the left hand (forefinger) as a reference and the proposed OPO is placed on the forefinger of the right hand or on the body part from which SpO_2 is measured. The subject stops breathing until the SpO_2 value of the commercial oximeter decreased and, at the same time, PPG signals are extracted from the red and green OLEDs of the OPOs (Fig. S8A). Based on these measured PPG signals, we obtained the so-called 'ratios of ratios (R)' per each PPG period and plot the SpO_2 measured with the commercial sensor vs. the experimentally obtained R value (Fig. S8B) (*11-13*). The example of calibration done for a forefinger is provided as Fig. S9.

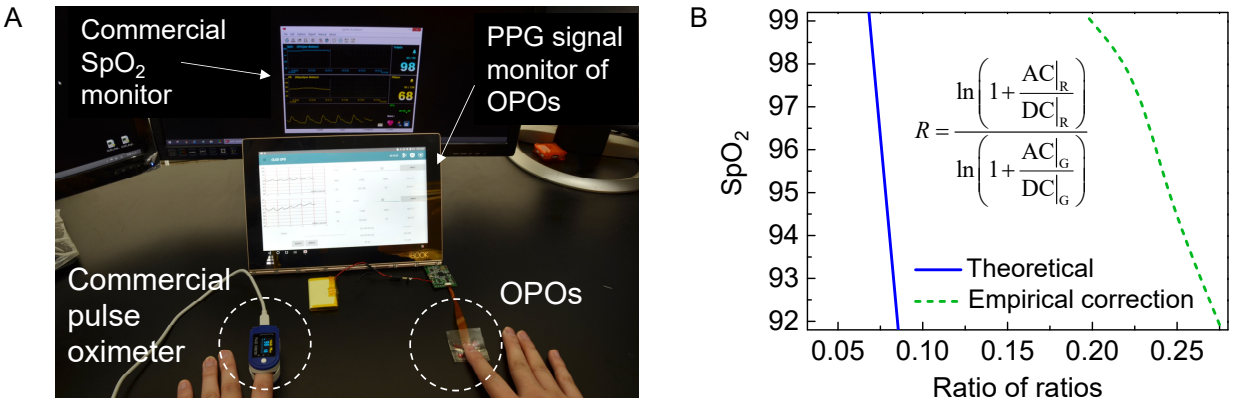

Fig. S8. Overview of the calibration method. (**A**) Picture of collecting PPG & SpO_2 data with a commercial SpO_2 sensor and the proposed OPO. (**B**) Measured SpO_2 vs. 'ratio of ratio' value (R) defined by: $R=\ln(1+AC/DC)|_{red}$ / $\ln(1+AC/DC)|_{green}$. The green dashed line shows the experimentally obtained R values. The theoretical curve (blue solid line) calculated by an ideal system following Beer-Lambert's Law is also provided for comparison. The extinction coefficients of Hb and HbO_2 in adults were borrowed from Zijlstra et al. Due to the reflective geometry and the effect of scattering, the experimentally obtained curves are different from the ideal theoretical curves, similarly to previous reports (*11-12*). Photo credit: Haechang Lee, KAIST.

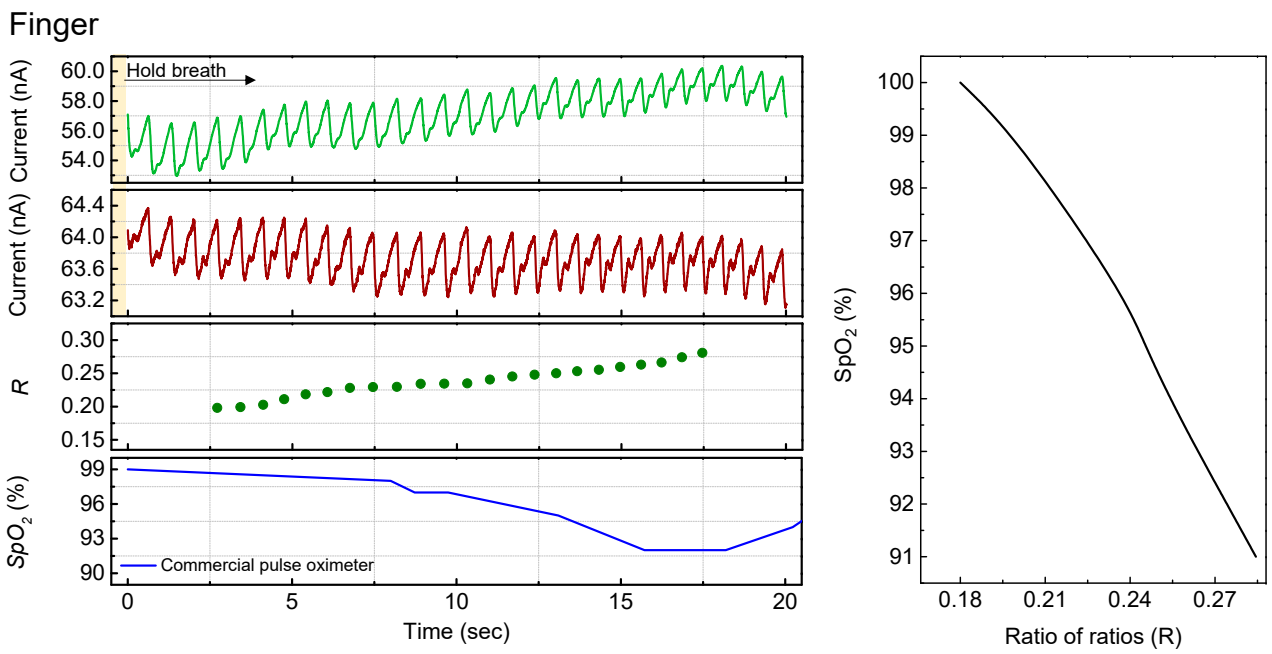

Fig. S9. Example of SpO_2 calibration done at a forefinger.